Micro-mechanics of electrostatically stabilized suspensions of cellulose nanofibrils under steady state shear flow†

F. Martoïa,[abcde] P. J. J. Dumont,‡*[abc] L. Orgéas,[de] M. N. Belgacem[abc] and J.-L. Putaux[fg]

In this study, we characterized and modeled the rheology of TEMPO-oxidized cellulose nanofibril (NFC) aqueous suspensions with electrostatically stabilized and unflocculated nanofibrous structures. These colloidal suspensions of slender and wavy nanofibers exhibited a yield stress and a shear thinning behavior at low and high shear rates, respectively. Both the shear yield stress and the consistency of these suspensions were power-law functions of the NFC volume fraction. We developed an original multiscale model for the prediction of the rheology of these suspensions. At the nanoscale, the suspensions were described as concentrated systems where NFCs interacted with the Newtonian suspending fluid through Brownian motion and long range fluid–NFC hydrodynamic interactions, as well as with each other through short range hydrodynamic and repulsive colloidal interaction forces. These forces were estimated using both the experimental results and 3D networks of NFCs that were numerically generated to mimic the nanostructures of NFC suspensions under shear flow. They were in good agreement with theoretical and measured forces for model colloidal systems. The model showed the primary role played by short range hydrodynamic and colloidal interactions on the rheology of NFC suspensions. At low shear rates, the origin of the yield stress of NFC suspensions was attributed to the combined contribution of repulsive colloidal interactions and the topology of the entangled NFC networks in the suspensions. At high shear rates, both concurrent colloidal and short (in some cases long) range hydrodynamic interactions could be at the origin of the shear thinning behavior of NFC suspensions.

1 Introduction

Cellulose nanofibrils (NFCs) are interesting biosourced building blocks, isolated from cellulose fibers in the form of slender nanofibers with outstanding mechanical properties.[1] These nanofibers can be used to manufacture many promising materials including yarns,[2,3] films,[4] aerogels[5] and (nano-)composites.[1,6] NFCs can be extracted from their native cellulosic fibers using various chemical and mechanical treatments.[1] Among them, one of the most efficient extraction routes is TEMPO-mediated oxidation[7,8]

[a] Univ. Grenoble Alpes, LGP2, F-38000 Grenoble, France.
  E-mail: pierre.dumont@insa-lyon.fr
[b] CNRS, LGP2, F-38000 Grenoble, France
[c] Agefpi, F-38000 Grenoble, France
[d] Univ. Grenoble Alpes, 3SR Lab, F-38000 Grenoble, France
[e] CNRS, 3SR Lab, F-38000 Grenoble, France
[f] Univ. Grenoble Alpes, CERMAV, F-38000 Grenoble, France
[g] CNRS, CERMAV, F-38000 Grenoble, France
† Electronic supplementary information (ESI) available. See DOI: 10.1039/c5sm02310f
‡ Present address: Université de Lyon, INSA-Lyon, LaMCoS CNRS UMR5259, F-69621 Villeurbanne Cedex, France.

which yields well-individualized NFCs while preserving a significant content of native crystalline cellulose. At low pH and high ionic strength, TEMPO-oxidized NFC aqueous suspensions exhibit heterogeneous and flocculated textures.[4,9–11] Materials processed with these NFCs have altered physical and mechanical properties.[4] On the contrary, at high pH and low ionic strength, NFC aqueous suspensions are homogeneous, nearly transparent and electrostatically stabilized by the presence of negatively charged carboxyl groups.[4,9,10] In these situations, NFC-based materials exhibit significantly enhanced[4] but not optimized end-used properties. Thus, it is crucial to understand and to control macroscale flow properties and flow-induced nanostructures of stabilized TEMPO-oxidized NFC suspensions during processing.[2,3,12,13]

Electrostatically stabilized TEMPO-oxidized NFC suspensions exhibit a very complex rheology.[14] These suspensions usually behave like thixotropic shear thinning and anisotropic yield stress fluids.[14–16] They combine typical rheological features of soft glassy materials[17] such as clay suspensions, concentrated emulsions and colloidal gels, but also typical features of colloidal and non-colloidal fiber suspensions such as carbon nanotube

and glass or biosourced fiber suspensions.[18] For example, during shearing, stabilized TEMPO-oxidized NFC suspensions exhibit heterogeneous flow properties,[14,16] which involves strain localization, shear banding, migration, segregation, and wall depletion, as well as potential structural rearrangement such as fiber orientation[12] and deformation, shear-induced rejuvenation and destructuration. The situation is even more complicated when NFC suspensions exhibit flocculated textures.[14,19] These suspensions are unstable and exhibit complex and heterogeneous flow kinematics under shear.[14,19] Hence, for all the aforementioned NFC suspensions, advanced rheometry setups and procedures are required to properly characterize their intrinsic bulk flow properties.[20–23]

Recent studies on NFC suspension rheology have reported that stabilized TEMPO-oxidized NFC suspensions behave at first order like Herschel–Bulkley fluids at the macroscale:[15,24]

$$\tau = \tau_0 + K\dot{\gamma}^n, \tag{1}$$

where τ_0, K and n are the macroscale shear yield stress, shear consistency and flow index, respectively, and where τ_0 and K are power-law functions of the volume fraction of NFC ϕ:

$$\tau_0 \propto \phi^e \text{ and } K \propto \phi^g, \tag{2}$$

where $2 < e < 3.5$ and $2 < g < 2.5$.

These approaches provide important general phenomenological trends but do not relate the macroscale rheology of NFC suspensions to their complex nanostructure and deformation nano-mechanisms. For that purpose, rare but interesting multiscale analyses have been developed for these biosourced fibrous systems.[24,25] For example, by performing shear tests with a vane rheometer at low shear rates with NFC suspensions (concentration ranging between 0.5 and 10 wt%), Varanasi et al.[25] used an excluded volume theory, namely the crowded number theory,[26] to estimate the mean NFC aspect ratio $r = l/d$ (where l and d are the mean NFC length and diameter, respectively) at the gel point, i.e., at the critical NFC volume fraction ϕ_c for which a yield stress τ_{0c} is first observed and for which NFCs form a cohesive connected fibrous network. This model enables the critical macroscale yield stress τ_{0c} to be related to the underlying nanoscale fibrous reinforcements of the NFC suspensions. However, this approach does not take into account neither the wavy nature of NFCs, nor their potential orientation[12] and deformation that could be induced during suspension flow (the crowded number being used in the isotropic case with the assumption of straight fibers[26]). Further, this model cannot explain the experimental trends which are observed in the concentrated regime, i.e., above the critical NFC concentration ϕ_c (see eqn (2)). It is also based on the extension of a theory initially developed for pulp fiber suspensions, i.e., for flocculated suspensions made of micrometric fibers. Thus, a more appropriate framework is required to analyze the rheology of stabilized colloidal NFC suspensions such as TEMPO-oxidized NFC suspensions.

Colloidal interactions are known to play a central role in the non-Newtonian behavior of soft-glassy systems, especially in the low shear strain regime or low shear rate regimes where these systems exhibit solid-like properties.[17,20,27–30] For instance, for a sufficiently high concentration of colloids, the macroscale yield stress τ_0 is often attributed to the formation of networks of strong colloidal interaction forces $\mathbf{f}^{col}$ that are able to restrain the Brownian forces $\mathbf{f}^B$ exerted by the suspending fluid on the elastic colloidal particles. In the case of repulsive colloidal systems such as the studied NFC suspensions, solid-like properties are closely related both to the topological arrangement and the geometry of colloids.[13,31] For slender wavy and entangled semi-flexible fibers, geometrical and topological effects are of great importance like in non-colloidal fibrous materials.[32,33] Hence, τ_0 is often related to a number of particle "bonds" B per unit area A of the sample and to a characteristic force f_c^{col} required to pull these bonds apart:[27,28]

$$\tau_0 \propto \frac{B f_c^{col}}{A}. \tag{3}$$

In general, the number of particle "bonds" B is estimated geometrically by using excluded volume approaches. This method was used in the random contact equation that was developed by Philipse[34] to estimate the average number of contacts per particle z in suspensions of randomly oriented rods. In addition, it is worth noting that other studies[28,35,36] showed that the range of characteristic forces f^c is in good agreement with the colloidal forces that are predicted by the classical DLVO theory developed by Derjaguin, Landau, Verwey and Overbeek.

At higher shear rates, i.e., in the liquid-like regime, other interaction forces also become significant during suspension flow.[20,27–29] Long-range hydrodynamic interactions $\mathbf{f}^{hl}$ occur between the suspending fluid and the particles far from particle contact zones and short-range hydrodynamic interactions $\mathbf{f}^{hs}$ occur when the particles are sufficiently close to each other, i.e., if their interparticle distance is in the order of the particle diameter.

For the two aforementioned flow regimes, the macroscale rheology depends both on the current microstructure of the suspension and its evolution during flow. A complete analytical treatment would be quite difficult, requiring a fine description of the microstructure and flow micro-mechanisms. For concentrated suspensions of anisotropic slender and semi-flexible particles such as NFCs, the situation is even more complicated because of the potential flow-induced deformation and rotation of these particles.

In parallel to studies dedicated to colloidal systems, other multiscale theories have been developed in the field of fiber-reinforced composite materials to predict the rheology of concentrated polymer and non-colloidal fiber suspensions. The resulting rheological models relate the macroscopic rheological behavior of the suspensions to the fiber geometry and the fibrous architecture, i.e., the content, distribution and orientation of fibers. These microstructural parameters are of first importance since they determine for example the number of fiber–fiber contacts per unit volume. These models also emphasize the role of contact micromechanisms in the regions of inter-fiber contacts. In non-colloidal fiber suspensions, these local forces result from potential (i) elastic deformation of the fibrous network, i.e., bending or twisting deformation of fibers between

contact points, (ii) dry Coulombic friction phenomena that are induced by the contacts between fibers, and (iii) lubrication interactions that are induced by shearing of thin suspending fluid zones in the vicinity of contact zones. These suspensions exhibit a highly anisotropic response that depends on the orientation state. Thus, the aforementioned models must be also accompanied by a set of fiber orientation equations for the prediction of the evolution of the anisotropy. Several theories have been purposely developed in the literature.[37–39] Most of them are based on the well-known Jeffery's equations.[40]

Recent studies have expanded these multiscale models to colloidal fibrous systems, for example carbon nanotube suspensions.[39] However, to the best of our knowledge, none of them properly encompasses the specific physics of colloidal forces between particles, and their critical role, in particular at low and moderate shear rates. Thus, the objective of the study was to build, from an experimental database and a theoretical framework inspired from those developed for non-colloidal and concentrated fibrous systems, a multiscale rheological model to emphasize the impact of the specific fibrous nanostructure and colloidal interactions of TEMPO-oxidized NFC suspensions on their shear rheology. The developed model is restricted to unflocculated suspensions, i.e., NFC suspensions at high pH and low ionic strength that are stabilized by repulsive colloidal interaction forces. In this context, we processed electrostatically stabilized TEMPO-oxidized NFCs[14] (Section 2). The geometry of these particles was finely characterized, and the macroscale shear rheology of TEMPO-oxidized NFC suspensions was investigated for various nanofiber contents (Section 3). This experimental database enabled a multiscale rheological model to be built, accounting for the fibrous nature of the considered suspensions and for the interaction forces between the fluid and the NFCs, namely Brownian and long range hydrodynamic interactions, and between contacting NFCs, namely repulsive colloidal and short range hydrodynamic interactions (Section 4). The nanoscale constitutive parameters of the model were identified using realistic elementary volumes of the fibrous nanostructures of NFC suspensions that were numerically generated. Finally, the relevance of the model was discussed (Section 5).

2 Materials and experimental procedures

2.1 Extraction of NFCs

TEMPO-oxidized NFC suspensions with 1 wt% of NFCs were obtained from a commercial eucalyptus bleached kraft pulp (Celbi, Portugal) using a processing route that has already been described by Martoïa et al.[14] A chromatography analysis of the suspending fluid showed that the solid content of residual sugars and oligomers (mainly hemicelluloses) was very low, i.e., approximately 70 mg L^{-1}. This suggests that only few residual oligomers were liberated during mechanical grinding, and that the studied NFCs could be considered to be suspended in a Newtonian matrix of water with a shear viscosity μ of 10^{-3} Pa s. Then, NFC suspensions at various concentrations ranging from

0.2 to 1 wt%, i.e., NFC volume fractions ϕ ranging from 0.0013 to 0.0067 (ϕ was estimated assuming a cellulose density ρ of 1500 kg m^{-3}), were prepared by diluting the initial NFC suspension with deionized water. All the suspensions were at pH 8.

2.2 Microscopy

The macro-, micro- and nano-scale morphologies of NFCs and NFC suspensions were investigated using various optical and electronic microscopy techniques. Natural and cross-polarized optical sources were used at meso- and micro-scales to assess the homogeneity of the processed suspensions. Micrographs were recorded in transmission mode on NFC aqueous suspensions diluted to 0.1 wt%, using an optical microscope (Axio Imager M1m, Zeiss) equipped with a camera (AxioCAM MRC5, Zeiss). A drop of the suspension was deposited into a cavity micro-slide (L4090 Agar Scientific, UK) that had a 18 mm diameter and a 1.5 mm depth. TEM observations were also carried out to analyze the nanoscale morphology of NFCs. TEM specimens were prepared by depositing a drop of NFC suspension at a concentration of 0.001 wt% onto glow-discharged carbon-coated electron microscopy grids. These specimens were then negatively stained with 2 wt% uranyl acetate and air-dried for a few minutes before being imaged using a Philips CM200 microscope operating at an accelerating voltage of 80 kV. Images were recorded on Kodak SO163 films.

2.3 Rheometry

The rheology of NFC suspensions was studied using a stress-controlled rheometer (MCR 301, Anton Paar Physica, Austria) equipped with a plate–plate geometry (diameter 25 mm, gap 1 mm) for the most concentrated suspensions ($\geq$0.3 wt%) and with a cone-plate geometry (diameter 50 mm, gap 150 μm) for the less concentrated suspensions (<0.3 wt%). To minimize wall slippage that often occurs when pasty materials are sheared,[16,17,20] the rheometer walls were covered with sandpaper (surface roughness 120 μm). All the measurements were performed at 20 °C with suspensions pre-sheared at 10^3 s^{-1} for 60 s. A glass solvent trap was systematically used to prevent water evaporation. As described by Martoïa et al.,[14] macroscale rheograms were obtained by sweeping down the macroscopic shear rate $\dot{\gamma}$ from 10^3 s^{-1} to 10^{-3} s^{-1} in 90 logarithmically-spaced steps for times of $\delta t = 50$ s (Fig. 2). This time resulted in a steady state response of the suspensions for each step.[14]

Typical macroscale flow curves that were obtained by following this procedure are shown in Fig. 2a. These flow curves exhibited a peculiar shape with two distinct regimes already observed in other colloidal systems.[41–43] As the macroscale shear rate was decreased from the high shear rate region, the macroscale shear stress progressively decreased to reach a horizontal plateau up to $\approx 10^{-1}$–10^0 s^{-1}. This plateau is usually considered to be close to the steady state macroscale yield stress τ_0.[17,20,44] In addition, it is interesting to notice that, within this first regime, the same suspension behaves identically when it is sheared inside a Couette geometry. Lowering the shear rate beyond the plateau yields a second regime with a remarkable decrease of the

macroscale shear stress that depends on the geometry of the rheometer (Fig. 2a).

To elucidate mesoscale flow mechanisms related to the macroscale rheology, we previously used the same Couette geometry coupled with an ultrasonic speckle velocimetry system (rheo-USV).[14,45] Regardless of the considered regime, the studied TEMPO-oxidized NFC suspensions were shown to exhibit heterogeneous mesoscale flows, with the occurrence of wall slippage, shear bands and in some cases plug-like flow bands. In the first flow regime, shear banding was moderate and no pronounced plug-like flow band was observed while sweeping down the shear rate: the recorded macroscale flow curves coincided, as a first order approximation, with that obtained using rheo-USV at the mesoscale. In the second flow regime, the decrease of the macroscopic shear stress τ was correlated with marked plug-like flow zones bands that spanned over the cell gap, as observed in other soft glassy materials.[17,42,44,46]

Thus, in light of these observations, only the first regime of the rheological data will be examined in the following sections, (i) assuming as a first approximation that the macroscale flow curves are sufficiently representative of the bulk rheology of the NFC suspensions, (ii) adopting the methodology reported in other studies[20,47] to analyze and discuss, from a phenomenological standpoint, flow curves using a Herschel–Bulkley approach, (eqn (1), Fig. 2a and b).

3 Experimental results

3.1 Multiscale structure of the processed NFCs

From the multiscale observations performed on the TEMPO-oxidized NFC suspensions (Fig. 1), several relevant remarks can be drawn. First, as shown in the inset picture in Fig. 1a, the processed TEMPO-oxidized NFC suspensions were stable, i.e., they did not exhibit flocculated textures. This stability was ensured by the presence of carboxylate groups [–COO$^-$] introduced at the surface of NFCs during the TEMPO treatment: the content of carboxyl groups [–COOH] determined by conductimetric titration Γ_{COOH} was 1.45 mmol g^{-1}, whereas it was only 0.05 mmol g^{-1} for native eucalyptus fibers. Thus, at the suspension pH, i.e. at pH 8, close to the pK_a of the acid–base pair (p$K_a \approx 8$), carboxyl groups were partially dissociated into carboxylate groups. Note also that these suspensions remained stable and unflocculated under shear flow.[14,16] In addition, the observations under cross-polarized light shown in Fig. 1b revealed that the studied NFC suspensions did not exhibit pronounced birefringent textures. This was likely due to the very high aspect ratio of NFCs and their kinks (for example, see the micrographs shown in Fig. 1c and d) that did not enable the particles to easily self-assemble into well-ordered domains.

A finer analysis of the microstructures showed that the processed NFC suspensions were bi-disperse in size: they contained (i) sparse fibers close to their original dimensions (diameter $\approx$ 20 μm and length $\approx$ 600 μm, Fig. 1a), and (ii) a very large amount of small and slender individualized fibrils. Even if the precise determination of the size of these very
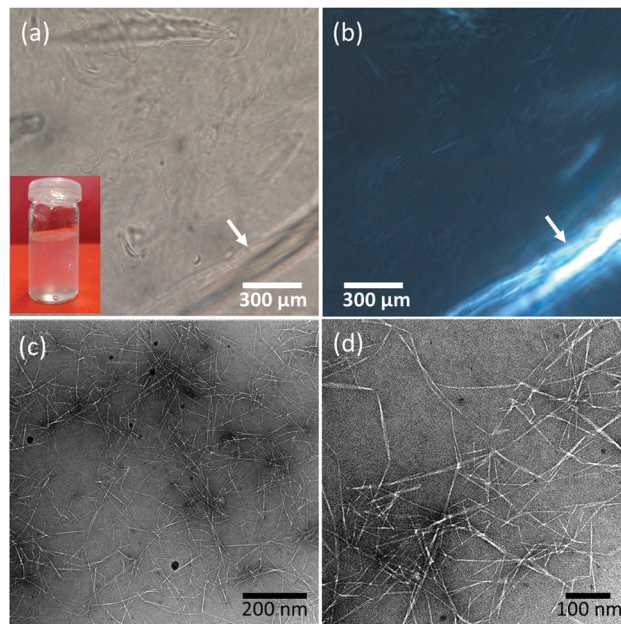

Fig. 1 Optical (a) and cross-polarized light micrographs (b) of a 0.1 wt% TEMPO-oxidized NFC suspension. The inset in (a) shows a 0.75 wt% TEMPO-oxidized NFC suspension. The white arrow indicates a partially fibrillated cellulose fiber, thus explaining the strong birefringence. (c and d) TEM micrographs of the dry suspensions after negative staining.

slender elements is still challenging, the dimensions of the NFCs were determined from the TEM images (Fig. 1c and d). We measured a mean diameter d of 4 nm and a mean length l of 1200 nm, i.e., a mean aspect ratio $r = l/d \approx 300$. It is worth noting that the diameter d and length l are in the same order of magnitude than that determined by Usov et al.[48] using AFM and TEM images from TEMPO-oxidized NFC suspensions extracted from wood fibers. Finally, TEM micrographs shown in Fig. 1c and d also revealed that the NFCs were tortuous and consisted of an assembly, on the average, of n_{seg} = 7 slender straight segments with a mean length l_{seg} = 169 nm interspersed with kinks or curved regions.[48] The mean misorientation angle θ_{seg} between each consecutive segment of a NFC was close to $\pi/8$ rad.[48]

3.2 Macroscale shear rheology

The values of τ_0, K, n of the Herschel–Bulkley model were fitted from the rheograms in Fig. 2b. They are reported in Fig. 3 as a function of the volume fraction of NFCs ϕ. The steady state yield stress τ_0 and the consistency K were power-law functions of ϕ (eqn (2) with power-law exponents e and g of 3.1 and 1.8, respectively). Keeping in mind the very small NFC volume fraction ϕ, these tendencies clearly emphasize a noteworthy thickening effect that can be directly related to the pronounced aspect ratio r of the studied NFCs ($\approx$ 300). These power-law exponents are in agreement with those previously reported for sheared TEMPO NFC suspensions.[15,24] However, some differences can be noticed. Particularly, the yield stress values shown in Fig. 3 are twice as large as those reported by Mohtaschemi et al.[24] This could be related to different rheometry procedures and/or differences in (i) the NFC microstructures and (ii) ionic
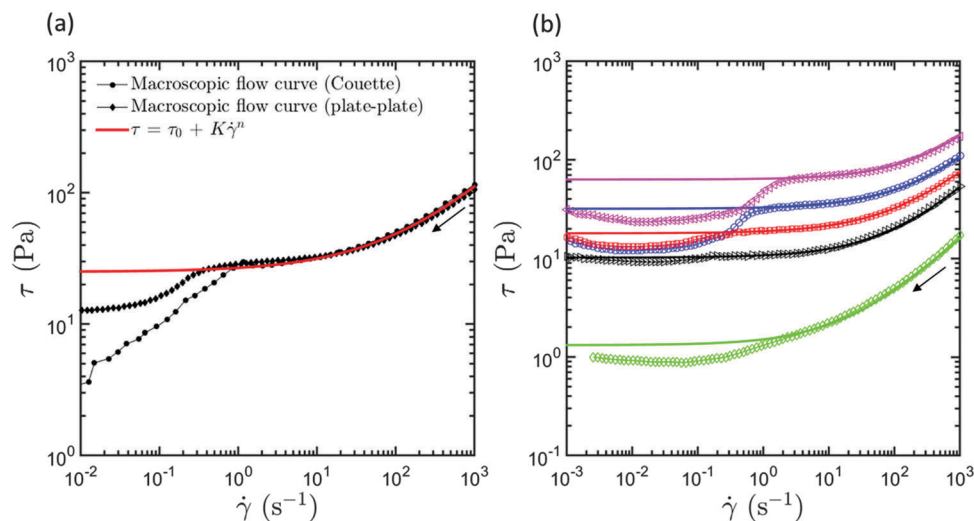
Fig. 2 (a) Flow curves obtained for a 0.85 wt% TEMPO-oxidized NFC suspension. The curve with black circle symbols represents a $\tau - \dot{\gamma}$ curve that was obtained using a Couette rheometer by sweeping down the macroscopic shear rate $\dot{\gamma}$ from 10^3 to 10^{-2} s^{-1} in 35 steps with times $\delta t = 50$ s. The curve with black diamond symbols represents a $\tau - \dot{\gamma}$ curve obtained using a plate–plate rheometer by sweeping down the macroscopic shear rate $\dot{\gamma}$ from 10^3 to 10^{-2} s^{-1} in 70 steps with times $\delta t = 50$ s. (b) Macroscopic flow curves obtained for various NFC suspensions concentrated at 0.3, 0.56, 0.7, 0.85, and 1 wt% using a plate–plate rheometer. In graphs (a) and (b), the solid lines represent the fits of the Herschel–Bulkley model (eqn (1)).

strength of the suspensions that control the aggregation state and stability of the ensuing colloidal systems. Finally, Fig. 3c shows that the flow index n was nearly independent of the NFC volume fraction ϕ and close to 0.6. In comparison, Mohtaschemi et al.[24] reported a slight decrease in the flow index n ($0.4 \leq n \leq 0.2$) as a function of ϕ ($0.0016 \leq \phi \leq 0.0067$).

4 Micromechanical analysis

As mentioned in the introduction, several experimental studies have already reported similar scaling laws to those shown in eqn (2) for other systems such as non-colloidal and colloidal fibrous suspensions[24–26,49] as well as colloidal gels[27,28] or other non-bonded fibrous media.[50–52] Other theoretical studies tried to recover the power-law exponents of these macroscale expressions using multiscale modeling approaches. For example, in an early theoretical study, van Wik[50] proved that the isostatic compression stress of non-bonded networks of randomly orientated, semi-flexible, slender, elastic, dry and straight fibers followed a scaling law similar to eqn (2) with a power-law exponent $e = 3$, neglecting friction forces at fiber contacts and assuming that fiber bending was the main fiber deformation mechanism. Later, Bennington et al.[49] adopted a similar approach to predict the shear yield stress in concentrated pulp fiber suspensions (assuming the suspension isotropy), leading to the same power-law exponent e. By revisiting the work of van Wik,[50] Toll and Månson[51] and Toll[52] emphasized the critical role of the fiber orientation on macroscale stresses. The authors showed that if $e = 3$ in the case of the compression of randomly oriented straight fibers, it could increase up to 5 for planar random fibrous networks, in accordance with experimental trends. Other network modeling approaches were also developed for polymeric concentrated fiber suspensions to predict the values

of the power-law exponent g observed with these systems in the viscous/high shear rate regime.[53–55] By assuming that (i) contact forces between fibers were induced by the shearing of the (non)-Newtonian suspending fluid in the vicinity of fiber–fiber contact zones and (ii) the connectivity the considered fibrous networks was well predicted by the tube model,[56] most of the authors found that g was equal to 2.

The aforementioned remarks show that the macroscale rheological properties of a wide class of concentrated fibrous soft materials are largely dominated at lower scales by (i) the geometry of fibers and their architecture (position, content and orientation), and (ii) the deformation mechanisms of the fibers and their contacts. Hence, in the following subsections, accounting both for the observed multiscale fibrous structures and macroscale rheological properties of NFC suspensions, we propose a multiscale model to link the small scale mechanics of these suspensions with their macroscale rheology.

4.1 Macroscale stresses and nanoscale interaction forces

Keeping in mind the experimental results in Sections 2 and 3, the considered TEMPO-oxidized NFC suspensions can be reasonably considered to be stabilized and unflocculated concentrated fiber suspensions with a Newtonian suspending fluid and semi-flexible slender elastic and curved nanofibers. The characteristic geometrical parameters of these elements, namely d, l, r, n_{seg}, l_{seg}, θ_{seg}, were estimated from the micrographs of Fig. 1c and d (Fig. 4 for idealized representations of the considered NFCs). At the microscale, typically the order of the nanofibril length l, nanofibrils form a connected fibrous network without microscale spatial heterogeneities (Fig. 1c and d, the rare pulp fibers were neglected for simplicity sake). During flow, nanofibrils translate, rotate and deform (see next subsection) with the suspending fluid while being subjected to four principal interaction forces.
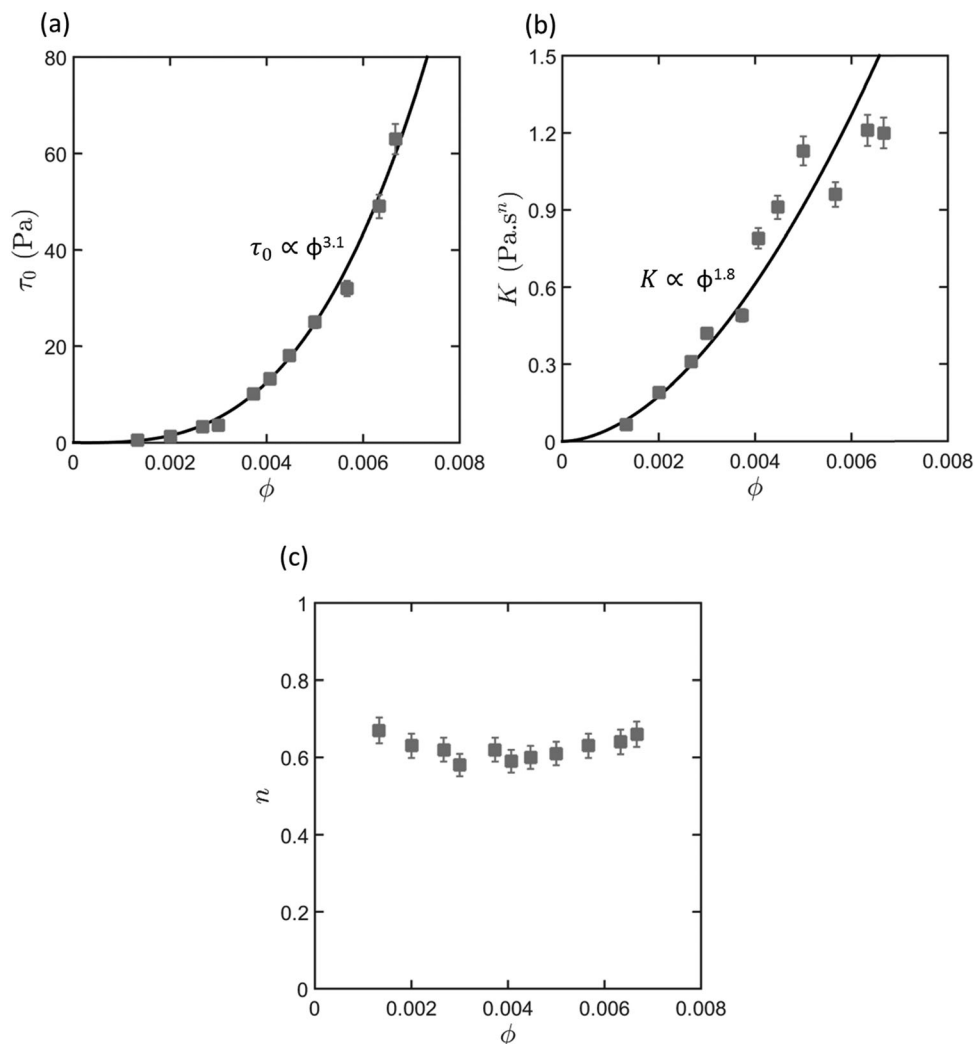
Fig. 3 Evolution of the parameters of the Herschel–Bulkley law as a function of the NFC content ϕ: steady state yield stress τ_0 (a), consistency K (b), and flow index n (c). Lines represent the power-law fits for the yield stress (a) and the consistency (b), respectively.

Two forces are related to their interactions with the suspending fluid far from fiber–fiber contact zones or bonds, namely forces $\mathbf{f}^{B}$ induced by the Brownian motion in the suspending fluid, and long range hydrodynamic viscous forces $\mathbf{f}^{hl}$ that are also induced by the fluid during the suspension flow. The two other forces, *i.e.*, $\mathbf{f}^{col}$ and $\mathbf{f}^{hs}$, occur in the bond zones and are related to colloidal and short range hydrodynamic viscous interactions, respectively. All the aforementioned nanoscale forces contribute to the macroscale Cauchy stress tensor $\boldsymbol{\sigma}$ of the considered suspensions. Assuming rationally that the suspensions are incompressible, the stress tensor $\boldsymbol{\sigma}$ can be expressed as follows:

$$\boldsymbol{\sigma} \approx -p\boldsymbol{\delta} + \boldsymbol{\sigma}^{B} + \boldsymbol{\sigma}^{hl} + \boldsymbol{\sigma}^{hs} + \boldsymbol{\sigma}^{col}, \tag{4}$$

where p is the incompressibility pressure, $\boldsymbol{\delta}$ the identity tensor, and where $\boldsymbol{\sigma}^{B}$, $\boldsymbol{\sigma}^{hl}$, $\boldsymbol{\sigma}^{hs}$ and $\boldsymbol{\sigma}^{col}$ represent macroscale stress contributions that are associated with the nanoscale forces $\mathbf{f}^{B}$, $\mathbf{f}^{hl}$, $\mathbf{f}^{hs}$ and $\mathbf{f}^{col}$, respectively. The links between the stress contributions, their associated interaction forces and the microstructure

of the suspensions can be deduced from theoretical or numerical upscaling processes.

The stress contribution $\boldsymbol{\sigma}^{B}$ is obtained from the expression reported for rod-like objects[57] with high aspect ratio r:

$$\boldsymbol{\sigma}^{B} = \frac{12}{\pi l^3}\phi r^2 k_B T\left(\mathbf{A} - \frac{1}{3}\boldsymbol{\delta}\right), \tag{5}$$

where k_B is the Boltzmann constant, T the suspension temperature and where $\mathbf{A}$ is the second order fiber orientation tensor[58] that is defined in a discrete form as follows:

$$\mathbf{A} = \frac{1}{N}\sum_{i=1}^{N} \mathbf{p}_i \otimes \mathbf{p}_i, \tag{6}$$

where the vectors $\mathbf{p}_i$ represent the mean unit tangent vectors of the N nanofibers i that are contained in a representative elementary volume of the suspension (Fig. 4).

A reasonable estimate of $\boldsymbol{\sigma}^{hl}$ induced by long range hydrodynamic forces is obtained from the micromechanical model
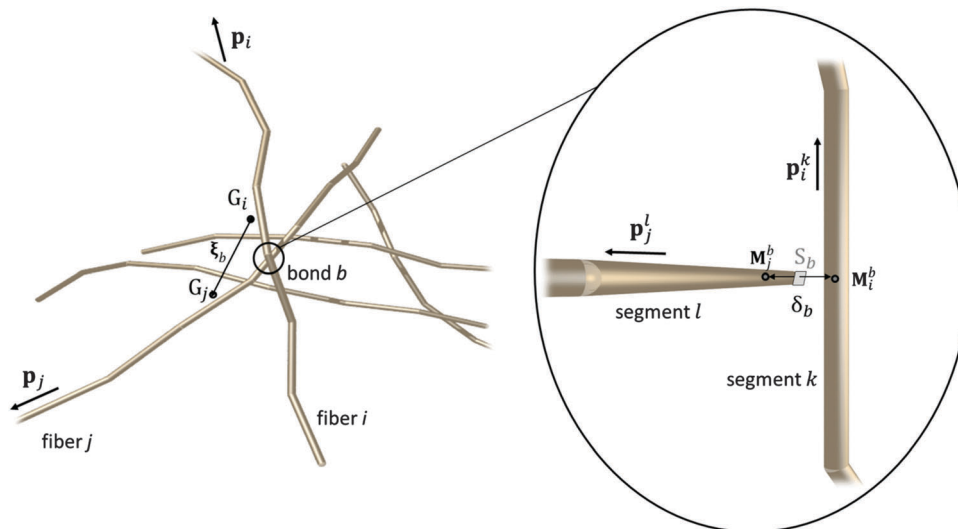
Fig. 4 Idealized representation of interacting NFCs and zoom on an interaction bond.

that has been developed by Lipscomb *et al.*[59] for Newtonian fiber suspensions in the semi-dilute regime:

$$\boldsymbol{\sigma}^{\mathrm{hl}} = 2\mu\mathbf{D} + 4\mu\phi\left(\mathbf{D} + \frac{r^2}{4\ln r}\mathbb{A}:\mathbf{D}\right), \quad (7)$$

where $\mathbf{D} = (\nabla\mathbf{v} + {}^t\nabla\mathbf{v})/2$ is the strain-rate tensor ($\mathbf{v}$ being the macroscale suspension velocity and $\nabla\mathbf{v} = \mathbf{v}\otimes\nabla$), and where $\mathbb{A}$ is the fourth order fiber orientation tensor,[58] defined as follows:

$$\mathbb{A} = \frac{1}{N}\sum_{i=1}^{N}\mathbf{p}_i\otimes\mathbf{p}_i\otimes\mathbf{p}_i\otimes\mathbf{p}_i. \quad (8)$$

The generic expressions of the stress contributions that are induced by viscous and colloidal bond forces are deduced from the following discrete forms:[54]

$$\boldsymbol{\sigma}^{\alpha} = \frac{2}{\pi l^3}\phi r^2 z^{\alpha}\xi_{\mathrm{c}}^{\alpha}f_{\mathrm{c}}^{\alpha}\frac{1}{B^{\alpha}}\sum_{b=1}^{B^{\alpha}}\boldsymbol{\xi}_{\mathrm{b}}^{\alpha*}\otimes\mathbf{f}_{\mathrm{b}}^{\alpha*} \quad (9)$$

where the notation "α" stands either for "hs", *i.e.*, short range hydrodynamic interactions, or for "col", *i.e.*, colloidal interactions. Hence, B^{α} is the total number of α-bonds in the representative volume, whereas z^{α} is the mean coordination number per nanofiber (or the mean number of nanofiber–nanofiber bonds per nanofiber) related to the α-bonds. In addition, $\boldsymbol{\xi}_{\mathrm{b}}^{\alpha*} = \mathbf{G}_i\mathbf{G}_j/\xi_{\mathrm{c}}^{\alpha}$ is the dimensionless placement vector related to the α-bond b, where, (i) as depicted in Fig. 4, $\mathbf{G}_i$ and $\mathbf{G}_j$ are the centers of mass of the two nanofibers i and j interacting at the α-bond b, and (ii) $\xi_{\mathrm{c}}^{\alpha}$ is the characteristic distance $\|\mathbf{G}_i\mathbf{G}_j\|$ between these nanofibers in the representative volume. Finally, $\mathbf{f}_{\mathrm{b}}^{\alpha*} = \mathbf{f}_{\mathrm{b}}^{\alpha}/f_{\mathrm{c}}^{\alpha}$ is the dimensionless α-bond force between the interacting nanofibers i and j, whereas the scalar f_{c}^{α} represents the characteristic value of the force magnitude $\|\mathbf{f}_{\mathrm{b}}^{\alpha}\|$ of the α-bond.

The above stress contributions emphasize the major and coupled roles exerted by the NFC suspension fibrous architectures and nanomechanics on their macroscale rheology. They can be calculated from proper estimates of the kinematics of NFCs (Section 4.2), associated to the fibrous nanostructures (Section 4.3) and the interaction forces at bonds.

During the suspension flow, two neighboring NFCs i and j interact *via* hydrodynamic interactions. When the distance between two nanofibers is sufficiently large, typically above the nanofiber diameter d, long range hydrodynamics interactions occur. Their effects on the macroscale stress tensor $\boldsymbol{\sigma}$ have been taken into account in the Newtonian stress contribution $\boldsymbol{\sigma}^{\mathrm{hl}}$ (eqn (7)). In other cases, *i.e.*, when the inter-fiber distance h^{hs} is below d, a hydrodynamic bond arises and short range hydrodynamic interactions occur.[27,28,60] In this small confined zone of nanoscale size, the molecules of the Newtonian suspending fluid are potentially subjected to complex flow mechanisms, leading to nanoscale lubrication forces $\mathbf{f}_{\mathrm{b}}^{\mathrm{hs}}$. Using small scale simulations with molecular dynamics simulation, Barrat and Bocquet[61] showed that the nanoscale efforts required to induce the flow of water molecules remained linear functions of the nanoscale flow rates of the fluid within confined nanoscale size geometries. Hence, for the studied TEMPO-oxidized NFC suspensions, a similar relationship is expected to occur between the nanoscale short-range hydrodynamic force $\mathbf{f}_{\mathrm{b}}^{\mathrm{hs}}$ and the relative velocity $\mathbf{v}_{\mathrm{b}}$ between two bonded nanofibers i and j at the hydrodynamic bond b. As the bonding zone depends on the relative orientation of the interacting nanofibers (Fig. 4), it was assumed that the short-range hydrodynamic force $\mathbf{f}_{\mathrm{b}}^{\mathrm{hs}}$ varies as a function of S_{b}, *i.e.*, the rhomb surface defined by the projection of the bonded nanofibers onto the normal plane of the bonding zone:[54,62]

$$S_{\mathrm{b}} = \frac{d^2}{\left\|\mathbf{p}_i^k\times\mathbf{p}_j^l\right\|}, \quad (10)$$

where the unit vectors $\mathbf{p}_i^k$ and $\mathbf{p}_j^l$ are the tangent vectors of the two fiber segments k and l, belonging to the contacting fibers i and j, respectively. Thus, the following linear form of $\mathbf{f}_{\mathrm{b}}^{\mathrm{hs}}$ is assumed:

$$\mathbf{f}_{\mathrm{b}}^{\mathrm{hs}} = \eta S_{\mathrm{b}}\Delta\mathbf{v}_{\mathrm{b}}, \quad (11)$$

where η can be regarded as an equivalent nanoscale bond viscosity. Hence, from the dimensionless framework in eqn (9), the above expression yields the following expression of the characteristic hydrodynamic interaction force f_c^{hs}:

$$f_c^{hs} = \eta S_{bc}\Delta v_{bc}, \quad (12)$$

where S_{bc} and Δv_{bc} are characteristic values of S_b and $\|\Delta\mathbf{v}_b\|$, respectively.

In the studied stabilized TEMPO-oxidized NFC suspensions, nanofibers also interact with their neighbors via repulsive colloidal long-range electrostatic forces $\mathbf{f}_b^{col}$. In a simplified view, these colloidal forces arise from the interpenetration of the ion layers that surround each NFC in colloidal bonding zones.[27,28,63] Thus, their intensity is expected to vary as a function of (i) the distance δ_b^{col} between the two nanofiber segments of nanofibers in interaction[27,28] and, (ii) the characteristic of the bond surface S_b (as for $\mathbf{f}_b^{hs}$). This leads to the following generic expression for the colloidal forces $\mathbf{f}_b^{col}$:

$$\mathbf{f}_b^{col} = \sigma^{col}(\delta_b^{col})S_b\frac{\Delta\mathbf{v}_b}{\|\Delta\mathbf{v}_b\|} \quad (13)$$

where σ^{col} is a colloidal force per unit of bond area. Its intensity depends on the NFC–NFC distance δ_b^{col} and the NFC ionic environment. Thus, introducing characteristic values σ_c^{col} and δ_c^{col} that are associated with σ^{col} and δ^{col}, respectively, the characteristic colloidal force f_c^{col} in eqn (9) is expressed as follows:

$$f_c^{col} = \sigma_c^{col}(\delta_c^{col})S_{bc}. \quad (14)$$

In colloidal systems where repulsive electrostatic forces dominate, the critical thickness h^{col} above which these interactions can be neglected is taken as the critical Debye screening length κ^{-1}. Several studied have shown the drastic effects of the Debye screening length κ^{-1} on the rheology of colloidal systems.[27,28,63,64] Thus, to determine the occurrence of colloidal interaction forces in the studied NFC systems, κ^{-1} was estimated using the methodology proposed by Ishii et al.[65] for aqueous TEMPO-oxidized NFC suspensions. Assuming that (i) the major ionic species of the aqueous NFC suspensions are Na^+ and COO^- (dissociated carboxylate groups), and (ii) neglecting the effect of counter ion condensation, κ^{-1} can be written as follows:

$$\kappa^{-1} \approx (8\pi l_B\rho N_A\Gamma_{COOH}\phi)^{-0.5}, \quad (15)$$

where l_B is the Bjerrum length (= 0.71 nm in water at 25 °C) and N_A the Avogadro's constant. According to the last expression, the Debye screening length κ^{-1} ranges between 2.5 nm (for ϕ = 0.0067) and 6 nm (for ϕ = 0.0013). It increases with decreasing NFC content ϕ and the dilution of NFC suspensions with pure water decreases the ionic concentration and thus the electric screening induced by these ions. Above this inter-fiber distance, colloidal interactions are supposed to be negligible, whereas below, interaction forces occur following the generic eqn (13).

4.2 Kinematics of NFCs

Eqn (11) and (13) show that it is necessary to get a relevant estimate of the relative velocity field $\mathbf{v}_b$ to assess the bonding forces f_b^{hs} and f_b^{col} and their associated macroscale stress contributions eqn (9). A possible method would consist in solving numerically momentum balances for all the NFCs contained in representative volumes.[66–68] This would provide exact values of $\mathbf{v}_b$ but would conduct to extremely long computation times. Instead, as commonly achieved to build relevant macroscale analytic estimates of the macroscale stress contributions,[39,53,55,75] nanoscale kinematical hypotheses were stated for the motion of NFCs during the suspension flow as described hereafter. Hence, the motions of the centers of mass $\mathbf{G}_i$ and $\mathbf{G}_j$ of two NFCs linked at bond b are affine functions of the macroscale velocity field $\mathbf{v}$ of the suspension, so that their relative velocity $\Delta\mathbf{v}_{bG}$ is expressed as follows:

$$\Delta\mathbf{v}_{b_G} = \mathbf{v}_{G_j} - \mathbf{v}_{G_i} \approx \nabla\mathbf{v}\cdot\mathbf{G}_i\mathbf{G}_j \quad (16)$$

In addition, we assumed that the deformation of NFCs during the suspension flow remains limited (this will be further discussed in the following section), so that at a first order approximation, NFCs are only subjected to translations and rotations.

Finally, the rotation of the NFCs was approached by Jeffery-based models.[37,40] Like in other fiber suspensions, the orientation of NFCs during flow drastically evolves,[3,12] which affects the suspension rheology (eqn (17)). The Jeffery-based models capture the main features of these evolutions. Thus, the rotation $\dot{\mathbf{p}}_i$ of the mean orientation vector $\mathbf{p}_i$ of the NFC i was expressed as:

$$\dot{\mathbf{p}}_i = \mathbf{W}\cdot\mathbf{p}_i + \lambda(\mathbf{D}\cdot\mathbf{p}_i)\cdot(\delta - \mathbf{p}_i\otimes\mathbf{p}_i)$$
$$+ D_r\frac{1}{\psi}\frac{\partial\psi(\mathbf{p})}{\partial\mathbf{p}}(\delta - \mathbf{p}_i\otimes\mathbf{p}_i), \quad (17)$$

where $\mathbf{W} = (\nabla\mathbf{v} - {}^t\nabla\mathbf{v})/2$ is the vorticity tensor and where λ is a shape factor[72] related to the geometry of the nanofibers (see Appendix S1 in ESI† for the used estimate). The last term of the right side of eqn (17) was initially proposed to account for Brownian rotary diffusion. It depends on the orientation distribution function $\psi(\mathbf{p})$ and its gradient and introduces a Brownian rotary diffusion coefficient D_r. In this study, this mechanism was a priori neglected. As pointed out later, Brownian effects are shown to play a secondary role on the rheology of the studied suspensions within the investigated testing conditions (Fig. 7). However, it is also well known that the rotation of a fiber in concentrated fiber suspensions is restrained by the presence of its neighbors.[68–71] To account for this phenomenon, we used Jeffery's equation purposely modified by Folgar and Tucker,[37] where the constant D_r in eqn (17) has been replaced by $C_I\sqrt{2\mathbf{D}:\mathbf{D}}$, and where the dimensionless interaction coefficient C_I[37,70] (typically ranging between 10^{-2} and 10^{-3}) gauges the importance of this effect.

Hence, the bond relative velocity $\mathbf{v}_b$ is expressed as follows, accounting for the aforementioned assumptions:

$$\Delta\mathbf{v}_b = \Delta\mathbf{v}_{bG} + \|\mathbf{G}_jM_j^b\|\dot{\mathbf{p}}_j - \|\mathbf{G}_iM_i^b\|\dot{\mathbf{p}}_i, \quad (18)$$

where M_i^b and M_j^b are located on the centerlines of the NFCs i and j, respectively, below and above the bond b (Fig. 4), and where $\mathbf{v}_{bG}$ and $\dot{\mathbf{p}}_k$ (k = i and j) are estimated using eqn (16) and (17), respectively.

4.3 Microstructure modeling

The experimental characterization of the microstructures formed by NFCs in water suspension (at rest but also during shearing) is a challenging problem. The morphology of NFCs is usually characterized using AFM and TEM images in a dry state (Fig. 1).[48] Few studies attempted to get structural information using NFC suspensions. Using small-angle X-ray scattering (SAXS) analyses, Torres-Rendon *et al.*[2] and Håkansson *et al.*[3] showed that NFCs aligned along the flow direction while being sheared in Poiseuille-like flow configurations with micrometric characteristic size. However, compared with non-colloidal fibrous systems[62,71,73] due to the nanoscale size of the NFCs, it is still difficult to get direct 3D images of their architectures in the suspensions. To circumvent this difficulty, we used a numerical generation process to mimic realistic suspension architectures, gathering both data obtained in Section 3 and Fig. 1 and those from the literature.[3,12] Thus, idealized three-dimensional NFC networks of representative elementary volume Ω of size $V = 1400 \times 1400 \times 1400$ nm^3 were generated extending the methodology proposed by Le Corre *et al.*[54] and Vassal *et al.*[74] This procedure is detailed in Appendix S2 in ESI.†

The connectivity of the generated NFC networks was assessed using a deterministic methodology based on a soft-core approach similar to that adopted in the tube-model approaches.[56,62] Note that these approaches are known to provide relevant estimation of the connectivity of fibrous systems with slender fibers.[62,73] Hence, a cylindrical control volume Ω_α of size $V_\alpha = \pi l_{seg}(d + h^\alpha)^2$ centered on the centerline of the segment k belonging to a fiber i was defined. The parameter h^α was the inter-bond distance above which the α-bond interaction forces could be considered to be negligible. The parameter h^α was d and $2\kappa^{-1}$ for hs or col bonds, respectively. Each fiber segments l that belonged to a fiber j whose centerline intersected the control volume Ω_α was added to the connectivity set of bonds B^α. It was checked that this generation procedure yielded the prediction of the analytical tube model for straight fibers ($\theta_{seg} = 0$).[56] In this case, the tube model prediction of the fiber coordination number z was

$$z = 4\left(\frac{d + h_\alpha}{d}\right)^2 \phi\left(\frac{2}{\pi}\frac{l}{(d + h_\alpha)}\Phi_1 + \Phi_2 + 1\right), \quad (19)$$

where the discrete expressions for the orientation functions Φ_1 and Φ_2 were defined as follows:

$$\Phi_1 = \frac{1}{N^2}\sum_{i=1}^{N}\sum_{i=1}^{N}\|\mathbf{p}_i \otimes \mathbf{p}_j\| \text{ and } \Phi_2 = \frac{1}{N^2}\sum_{i=1}^{N}\sum_{i=1}^{N}|\mathbf{p}_i \cdot \mathbf{p}_j|. \quad (20)$$

Fig. 5 and 6 show several microstructural descriptors that were calculated for the generated NFC networks with 3D random and for marked flow-induced orientations. To obtain these descriptors, 20 elementary volumes per investigated microstructure configuration were generated to get mean trends and error bars. The following comments can be drawn from these figures.

Fig. 5e and f show the distribution of the projected bonding areas S_b, *i.e.*, the rhomb surface formed by two mutually bonded

nanofibers, as defined in eqn (10). This geometric parameter only depended on the nanofiber orientation[76] and was not affected neither by the nanofiber content ϕ, nor by the thickness h^α. Thus, orientated fibrous networks induced an enlargement of the S_b-distribution towards higher values, leading to an increase in the mean characteristic value S_c.

The distribution of the distance $\|\xi_b^\alpha\|$ between centers of mass for the mutually interacting fibers is shown in the histograms of Fig. 5e and f. Regardless of the fibrous network orientation, the mean characteristic value ξ_c did not depend on h^α and was close to $l/3$, even if the shapes of the distribution functions exhibited some slight differences. Others numerical experiments (not shown here) revealed that ξ_c was mainly affected by nanofiber clustering,[76] *i.e.*, the spatial distribution of the centers of mass G_i in Ω, and by the NFC waviness that was controlled by θ_{seg}.

Fig. 6a and b shows the evolution of the mean coordination numbers z^α as a function of the NFC content ϕ. Regardless of the type of α-bonds, namely hydrodynamic hs, colloidal col or purely geometrical 0 (corresponding to $h^0 = 0$) bonds, z^α (i) reached non negligible values even at the very low investigated NFC contents, (ii) and drastically increased with the NFC content ϕ. Considering eqn (9), this effect is expected to severely increase bond stress contributions. In accordance with eqn (20) and (15), the mean coordination numbers z^α were affine or power-law type (with a power-law exponent close to 0.65) functions of ϕ for hydrodynamic or geometrical bonds, and for colloidal bonds, respectively. Note also that, regardless of the NFC orientation and content, the coordination numbers were much higher for hs and col-bonds than for the purely geometrical case.

Although an increase in S_c is observed with increasing the NFC orientation (Fig. 5e and f), orientated fibrous networks exhibited in the same time much lower coordination numbers z^α (Fig. 6). These combined and competing effects could alter the bond stress contributions (eqn (9)). In addition, Fig. 6 shows that the NFC waviness has an important effect on the network connectivity. This effect is limited for 3D microstructures (Fig. 6a), whereas a noteworthy increase in the mean coordination number with the NFC waviness is observed for orientated microstructures (Fig. 6b).

5 Model prediction and discussion

From the experimental microstructure measurements combined with the analytical and numerical developments presented in the two previous sections, stress contributions involved in eqn (4) were assessed and compared with rheometry results (Section 3). For that purpose, the steady state flow curves shown in Fig. 2 were fitted using eqn (5–9) and the generated flow-induced microstructures (Section 4). This approach enabled the forces f_c^{col} and f_c^{hs} to be determined. The two graphs shown in Fig. 7a and b illustrate the relevance of this procedure for a low and a high NFC content ϕ, respectively. The model prediction fits fairly well the experimental trends, namely the occurrence of a steady state macroscale yield stress τ_0 at low macroscale shear
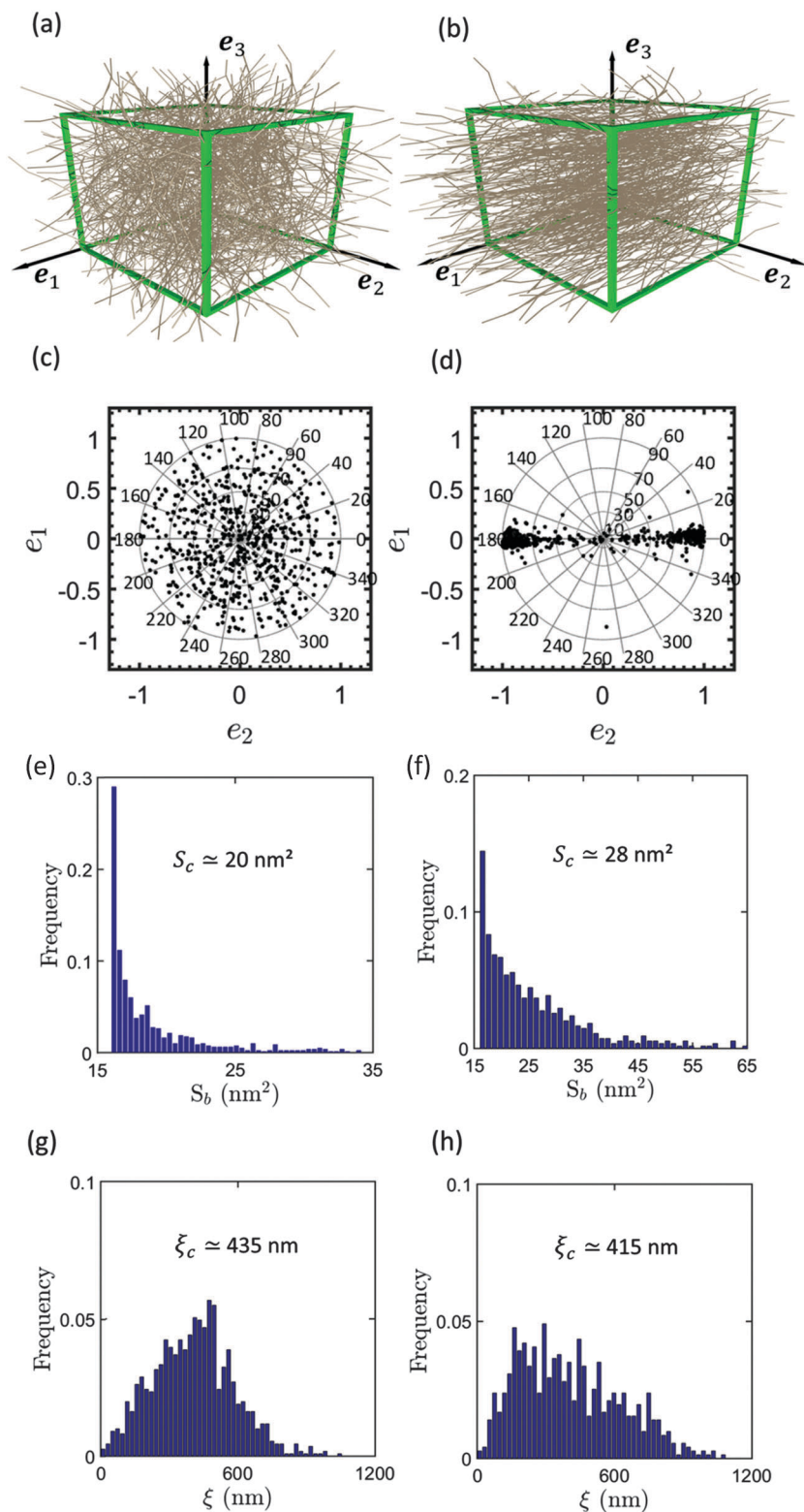
Fig. 5   Example of two idealized NFC networks for a nanofiber content $\phi = 0.004$ with 3D random orientation (a) and flow-induced orientation (b). For both types of microstructures, the orientation vectors $\mathbf{p}_i$ of each tortuous NFC i were represented using a stereographic projection (pole figure of orientation) along the e_3-direction (c and d). Typical distribution histograms of the projected bonding area S_b (e and f) and of the distance $\|\xi_b^\alpha\|$ between the centers of mass of interacting NFCs (g and h).

rates $\dot{\gamma}$, with a progressive shear thinning behavior as $\dot{\gamma}$ is increased. The increase of τ_0 with ϕ is also well reproduced by the model, as illustrated in Fig. 7. Fig. 7a and b also shows the evolution of the different stress contributions used in
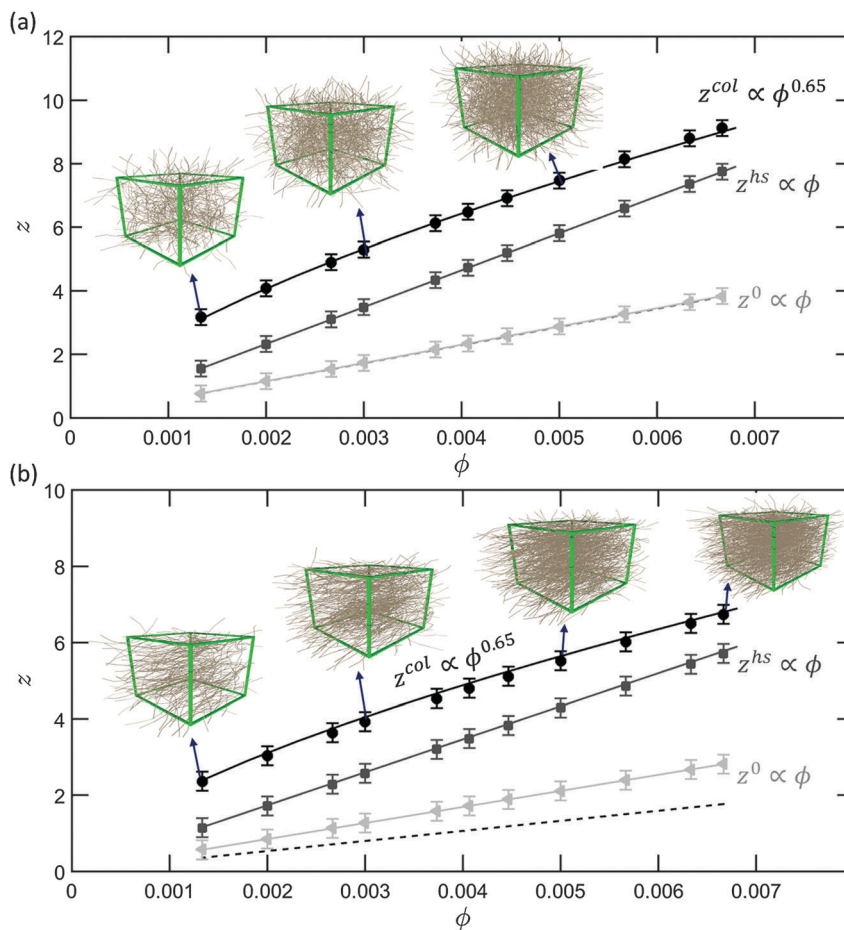
Fig. 6 Evolution of the mean coordination numbers z^α as a function of the NFC content ϕ for NFC architectures with various interaction thicknesses h^α (namely $h^0 = 0$, $h^{hs} = d$, $h^{col} = 2\kappa^{-1}$), NFC waviness ($\theta_{seg} = \pi/8$), for 3D random orientations (a) or flow-induced orientations (b). In both graphs, the dashed lines represent the evolution of the mean coordination numbers z^0 for straight NFCs ($\theta_{seg} = 0$) and ($h^0 = 0$).

eqn (4) to compute the macroscale steady state shear stress τ. Several interesting remarks listed in the following paragraphs can be drawn, independently from the considered nanofiber orientation.

Regardless of the shear rate and the NFC content, the Brownian shear stress contribution τ^B was always at least two decades lower than the experimental values recorded for τ. Accordingly, this result demonstrates that Brownian motion and its stress-induced contribution play a minor role in the rheology of the stabilized TEMPO-oxidized NFC suspensions, at least for the studied flow conditions. This result also supports the *a priori* assumption, stated in Section 4.2, that the flow-induced evolution of the NFC orientation could be predicted using a modified Jeffery's equation without Brownian diffusion term.

As expected, long range hydrodynamic interactions and their macroscale stress contributions τ^{hl} increased linearly as a function of $\dot{\gamma}$. The shear stress τ^{hl} was very small at low shear rates, *i.e.*, in the same order of magnitude as the Brownian stresses. At the highest shear rate (10^3 s^{-1}), its magnitude represented $\approx 20\%$ to $\approx 2\%$ of the macroscale shear stress as the NFC content was increased from 0.0013 to 0.0067. Thus, at high shear rates and low fiber contents, long range hydrodynamic

interactions contributed to the overall suspension stress. Otherwise, they have a second order effect. Together with the conclusions drawn in the previous point, this also suggests that both short range hydrodynamics and colloidal interactions mainly govern the rheology of the stabilized TEMPO-oxidized NFC suspensions.

Fig. 7a and b shows that the short range stress contribution τ^{hs} increased linearly as a function of $\dot{\gamma}$. This property is directly connected to the Newtonian expression of the forces $\mathbf{f}_b^{hs}$ (see eqn (11)). Using a rigorous upscaling process, *i.e.*, without the *a priori* affine assumption eqn (16), Le Corre *et al.*[77] theoretically proved that for such Newtonian interaction forces, the macroscale stress tensor $\boldsymbol{\sigma}^{hs}$ was a linear function of the macroscale strain rate tensor $\mathbf{D}$. In addition, Fig. 7a and b also shows that τ^{hs} is in the same order of magnitude as τ^{hl} for the lowest NFC content, whereas, for the highest contents, τ^{hs} was at least ten times higher, showing that τ^{hl} mainly contributed to the viscous behavior of the suspensions as the shear rate was increased.

The colloidal stress contribution τ^{col} was the major stress contribution at low shear rates (Fig. 7a and b): a sufficient macroscale external stress is required to overcome repulsive
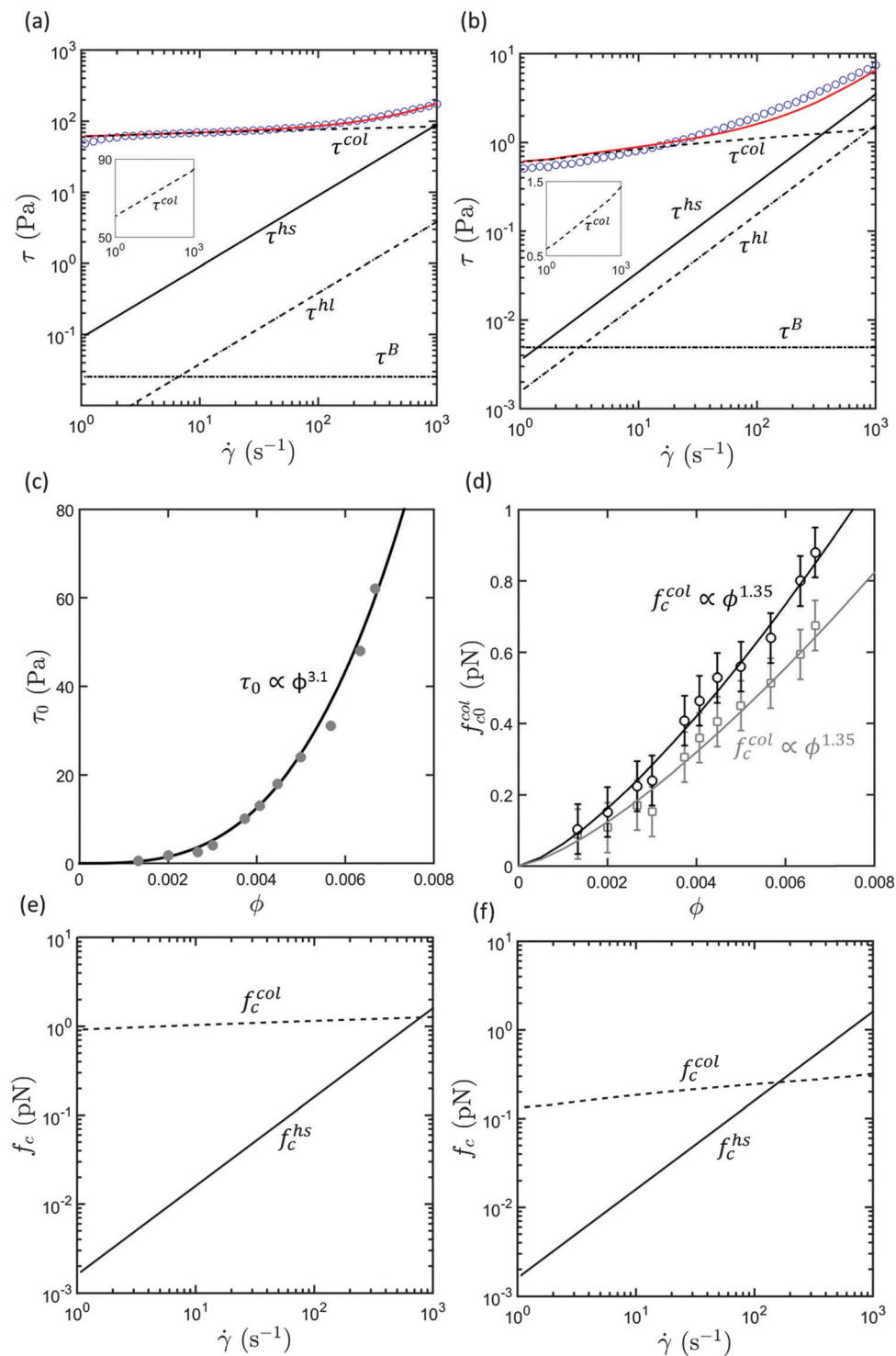
Fig. 7 (a and b) Macroscopic steady state shear stress as a function of the shear rate (curves with blue circle symbols) obtained for two TEMPO-oxidized NFC suspensions ($\phi = 0.0067$ and $\phi = 0.0013$), and prediction of the micromechanical (continuous red lines). The other lines represent the contributions that are induced by the Brownian motion τ^B, long and short hydrodynamic interactions τ^{hl}, τ^{hs} and colloidal interactions τ^{col}. (c) Prediction of the dynamic yield stress τ_0 of the micromechanical model. (d) Evolution of the characteristic colloidal force f_c^{col} as a function of the NFC content ϕ for random (grey color) and orientated fibrous microstructures (black color). (e and f) Predictions of the characteristic colloidal f_c^{col} and short hydrodynamic forces f_c^{hs} as a function of $\dot{\gamma}$ for two TEMPO-oxidized NFC suspensions ($\phi = 0.0067$ and $\phi = 0.0013$).

colloidal forces to continuously extract NFCs from their current network configuration towards a new one with identical steady state structure descriptors.

The physical origins of the shear thinning behavior observed in colloidal systems are multiple, and still constitute an open question.[29] In the developed model, the potential origin of the

shear thinning behavior of NFC suspensions could be the simultaneous occurrence of colloidal and short (in some cases long) range hydrodynamic interactions in a high shear rate regime that ranged from 10 to 10^3 s^{-1}.[27,28]

The conclusions drawn from the previous points are still valid when the model was fitted for 3D random fibrous networks, *i.e.*, when the potential flow-induced orientation was not taken into account.

To further discuss the results and their relevance, Fig. 7d shows the evolution of the characteristic colloidal forces f_c^{col} at low shear rates as a function of the NFC content ϕ. The estimated colloidal forces were very small (<1 pN) and fell within the range that could be expected from (i) the idealized DLVO theory with the considered electrostatic potentials,[78,79] and (ii) from the measured forces for model colloidal systems.[78] Fig. 7d also shows the effect of the orientation of the NFC fibrous networks since flow-induced orientated structures yielded colloidal forces twice higher than for 3D random networks. This effect could be related to the lower coordination number z^{col} for the orientated networks (Fig. 6). In addition, Fig. 7d shows the pronounced increase of f_{c0}^{col}, as a function of ϕ at low shear rates. Regardless of the fibrous orientation, the same relationship $f_{c0}^{col} \propto \phi^{1.35}$ was obtained. This trend could be related to two combined effects: the decrease in the Debye length κ^{-1} (see eqn (15)) and the variations in the electrostatic interaction potentials with increasing the NFC content ϕ.

Fig. 7a, b, e and f show that the shear stress τ^{col} and colloidal forces f_c^{col} increased with increasing the shear rate $\dot{\gamma}$. As expected, the same trend is obtained for long and short range hydrodynamic interaction forces (Fig. 7e and f). These nanoscale interactions may induce the deformation of NFCs (assumed to remain limited in the developed model). This would lead to an increase in the elastic energy stored into the NFCs and to a decrease in the inter-bond distance δ^{col}, *i.e.*, to an increase in the electrostatic forces and consequently in the shear stress τ^{col}. This scenario should be confirmed using for example direct simulation at the NFC scale.

Finally, the relevance of the model was assessed in regards with the network connectivity. A macroscale shear yield stress at low shear rates results from the existence of a continuous network of connected colloidal nanofibers along the sheared thickness of the suspension. This condition is fulfilled when the mean coordination of the NFC network is above the geometrical percolation threshold, *i.e.*, above a critical coordination number z_c. Berhan and Sastry[80] studied the percolation threshold for networks of helical fibers using a generation procedure that was similar to that of this study. For fiber networks with 3D random orientation, these authors have shown that z_c can be expressed as follows:

$$z_c = 1 + c_1(2r)^{-c_2}, \qquad (21)$$

where $c_1 = 5.231$ and $c_2 = 0.569$ for straight fibers and $c_1 = 11.156$ and $c_2 = 0.664$ for curved fibers that are similar to the studied NFCs. In both cases, z_c is close to 1.15. Further, Balberg *et al.*[81] also demonstrated that the percolation threshold z_c for orientated straight fibers in the perpendicular direction to the fiber

alignment was close to that for isotropic networks. This prediction was obtained using a excluded volume theory that was similar to the tube model, replacing the cylinder by a spherocylinder. Consequently, a critical percolation threshold is expected to occur when $z_c^0 > 1.15$ for the studied NFC suspensions. Fig. 6b shows that this condition was not fulfilled for orientated networks and for $\phi < 0.003$ when the connectivity was estimated using the geometrical coordination number z^0. On the contrary, a shear yield stress should practically exist for all NFC contents, accounting for the colloidal forces. Indeed over the investigated range of NFC content, the connectivity z^{col} was above the critical coordination number z_c^{col}, that ranged between 1.43 and 1.27 as the NFC content ϕ increased from 0.0013 to 0.0067 (note that to estimate values of z_c^{col}, we took into account the NFC diameter and the Debye length in the estimate of the aspect ratio r in eqn (21), *i.e.*, $r = l/(d + h^{col})$).

A similar reasoning applies for the short range hydrodynamic forces. In this case, the percolation should be attained for $z_c^h > 1.25$. Fig. 6b shows that the connectivity z^{hs} was also above this critical coordination number except for the lowest investigated NFC content.

6 Conclusion

The objective of this study was to relate the macroscale rheology of NFC suspensions to their complex nanostructure and deformation nano-mechanisms. For that purpose, we characterized the shear rheology of stabilized and unflocculated NFC colloidal suspensions, namely TEMPO-oxidized NFC aqueous suspensions at high pH and low ionic strength. The geometry of NFCs was characterized from TEM images, showing that NFCs could be considered to be slender and wavy fibers with nanometric diameters. The steady state rheology of the NFC suspensions was studied using plate–plate and Couette rheometers, showing that the suspensions behaved as Herschel–Bulkley fluids with a shear-thinning behavior. The yield stress and the consistency of these suspensions were power-law functions of the NFC content.

Besides, an original multiscale model was developed for the prediction of the observed experimental trends. NFC suspensions were considered to be stabilized and unflocculated colloidal and concentrated suspensions. The suspending fluid was seen as Newtonian and NFCs were considered to be slender and wavy nanofibers subjected to translation and rotation motions. The model took into account the contributions to the macroscale rheology of NFC suspensions of the interaction forces between the fluid and the NFCs, namely Brownian and long range fluid–NFC hydrodynamic interactions, as well as nanoscale short range hydrodynamic and repulsive colloidal interactions between NFCs. The nanoscale constitutive parameters of the model were identified using the experimental database and realistic 3D networks of NFCs that were numerically generated to mimic the nanostructures of NFC suspensions under shear flow.

For the studied flow conditions, the model prediction showed that both short range hydrodynamics and colloidal interactions mainly governed the rheology of TEMPO-oxidized NFC suspensions.

On the contrary, Brownian motion, and its stress-induced contribution only played a minor role in the rheology of TEMPO-oxidized NFC suspensions. Similarly, the contribution of long range hydrodynamic interactions was minor, except for high shear rates and low NFC contents. The main contributor to the viscous macroscopic stress was short range hydrodynamic interactions. At low shear rates (≈ 1 s^{-1}), colloidal interactions between NFCs were the major stress contribution and could be at the origin of a steady state yield stress. At high shear rates, the contribution of colloidal interactions was in the same order of magnitude than that of short (in some cases long) range hydrodynamic interactions. The simultaneous occurrence of colloidal and short (in some cases long) range hydrodynamic interactions could be at the origin of the shear thinning behavior of NFC suspensions for shear rates that ranged from 10 to 10^3 s^{-1}.

The model enabled both characteristic colloidal and short range hydrodynamic forces to be estimated. The estimated colloidal forces were very small: approximately 1 pN for the highest shear rates. These forces were in the same order of magnitude as those that could be expected from the DLVO theory or from measured forces for model colloidal systems.[10,78]

The suitability of the model was also assessed in regards with the NFC network connectivity. In the entire range of investigated NFC contents, the mean coordination number of the NFC network estimated by taking into account the Debye length was higher than the theoretical percolation threshold which represents the lower limit for the existence of a yield shear stress.

The proposed multiscale model could be enhanced to extend its validity domain. For example, it could be interesting to take into account the bending and the twisting of NFCs induced by colloidal and hydrodynamic forces. Taking into account these mechanisms into a semi-analytical model still constitutes a challenging task for networks of slender fibers with long inter-bond distances, such as the studied NFC networks.[32] Direct simulations at the NFC scale would probably provide useful information. Attractive colloidal forces could also be taken into account to model the rheology of flocculated systems. This is a very challenging task. Despite recent progress on the description of the motion of rigid clusters made of non-Brownian and non-colloidal straight fibers in dilute regime,[82] this remains an open question for concentrated colloidal fiber suspensions.

Acknowledgements

References

1 A. Dufresne, *Nanocellulose: From Nature to High Performance Tailored Materials*, Walter de Gruyter, 2012.

2 J. G. Torres-Rendon, F. H. Schacher, S. Ifuku and A. Walther, *Biomacromolecules*, 2014, **15**, 2709–2717.

3 K. M. O. Håkansson, A. B. Fall, F. Lundell, S. Yu, C. Krywka, S. V. Roth, G. Santoro, M. Kvick, L. Prahl Wittberg, L. Wågberg and L. D. Söderberg, *Nat. Commun.*, 2014, **5**, 4018.

4 A. J. Benítez, J. Torres-Rendon, M. Poutanen and A. Walther, *Biomacromolecules*, 2013, **14**, 4497–4506.

5 Y. Kobayashi, T. Saito and A. Isogai, *Angew. Chem.*, 2014, **126**, 10562–10565.

6 R. J. Moon, A. Martini, J. Nairn, J. Simonsen and J. Youngblood, *Chem. Soc. Rev.*, 2011, **40**, 3941–3994.

7 T. Saito, Y. Nishiyama, J.-L. Putaux, M. Vignon and A. Isogai, *Biomacromolecules*, 2006, **7**, 1687–1691.

8 A. Isogai, T. Saito and H. Fukuzumi, *Nanoscale*, 2011, **3**, 71–85.

9 K. Sim, J. Lee, H. Lee and H. J. Youn, *Cellulose*, 2015, **22**, 3689–3700.

10 H. Fukuzumi, R. Tanaka, T. Saito and A. Isogai, *Cellulose*, 2014, **21**, 1553–1559.

11 A. B. Fall, S. B. Lindström, O. Sundman, L. Ödberg and L. Wågberg, *Langmuir*, 2011, **27**, 11332–11338.

12 H. Sehaqui, N. Ezekiel Mushi, S. Morimune, M. Salajkova, T. Nishino and L. A. Berglund, *ACS Appl. Mater. Interfaces*, 2012, **4**, 1043–1049.

13 A. B. Fall, S. B. Lindström, J. Sprakel and L. Wågberg, *Soft Matter*, 2013, **9**, 1852–1863.

14 F. Martoïa, C. Perge, P. J. J. Dumont, L. Orgéas, M. A. Fardin, S. Manneville and M. N. Belgacem, *Soft Matter*, 2015, **11**, 4742–4755.

15 M. Mohtaschemi, K. Dimic-Misic, A. Puisto, M. Korhonen, T. Maloney, J. Paltakari and M. J. Alava, *Cellulose*, 2014, **21**, 1305–1312.

16 O. Nechyporchuk, M. N. Belgacem and F. Pignon, *Cellulose*, 2015, **22**, 2197–2210.

17 D. Bonn, J. Paredes, M. M. Denn, L. Berthier, T. Divoux and S. Manneville, arxiv150205281 Cond-Mat, 2015.

18 A. W. K. Ma, M. R. Mackley and S. S. Rahatekar, *Rheol. Acta*, 2007, **46**, 979–987.

19 T. Saarinen, S. Haavisto, A. Sorvari, J. Salmela and J. Seppälä, *Cellulose*, 2014, **21**, 1261–1275.

20 P. Coussot, *Rheometry of Pastes, Suspensions, and Granular Materials: Applications Industry and Environment*, John Wiley & Sons, 2005.

21 P. Coussot, *J. Non-Newtonian Fluid Mech.*, 2014, **211**, 31–49.

22 P. C. F. Møller, J. Mewis and D. Bonn, *Soft Matter*, 2006, **2**, 274–283.

23 G. Ovarlez, S. Cohen-Addad, K. Krishan, J. Goyon and P. Coussot, *J. Non-Newtonian Fluid Mech.*, 2013, **193**, 68–79.

24 M. Mohtaschemi, A. Sorvari, A. Puisto, M. Nuopponen, J. Seppälä and M. J. Alava, *Cellulose*, 2014, **21**, 3913–3925.

25 S. Varanasi, R. He and W. Batchelor, *Cellulose*, 2013, **20**, 1885–1896.

26 R. J. Kerekes, *Nord. Pulp Pap. Res. J.*, 2006, **21**, 598–612.

27 W. B. Russel, D. A. Saville and W. R. Schowalter, *Colloidal Dispersions*, Cambridge University Press, 1992.

28 J. Mewis and N. J. Wagner, *Colloidal Suspension Rheology*, Cambridge University, 2012.

29 P. Coussot, *Soft Matter*, 2007, **3**, 528–540.

30 M. J. Solomon and P. T. Spicer, *Soft Matter*, 2010, **6**, 1391–1400.

31 S. R. Raghavan and J. F. Douglas, *Soft Matter*, 2012, **8**, 8539–8546.

32 R. C. Picu, *Soft Matter*, 2011, **7**, 6768–6785.

33 D. Rodney, B. Gadot, O. R. Martinez, S. R. du Roscoat and L. Orgéas, *Nat. Mater.*, 2016, **15**, 72–77.

34 A. P. Philipse, *Langmuir*, 1996, **12**, 1127–1133.

35 A. S. Michaels and J. C. Bolger, *Ind. Eng. Chem. Fundam.*, 1962, **1**, 153–162.

36 R. J. Hunter and S. K. Nicol, *J. Colloid Interface Sci.*, 1968, **28**, 250–259.

37 F. Folgar and C. L. Tucker, *J. Reinf. Plast. Compos.*, 1984, **3**, 98–119.

38 D. L. Koch, *Phys. Fluids*, 1995, **7**, 2086–2088.

39 G. Natale, M. C. Heuzey, P. J. Carreau, G. Ausias and J. Férec, *AIChE J.*, 2014, **60**, 1476–1487.

40 G. B. Jeffery, *Proc. R. Soc. London, Ser. A*, 1922, **102**, 161–179.

41 G. V. Vinogradov, G. B. Froishteter, K. K. Trilisky and E. L. Smorodinsky, *Rheol. Acta*, 1975, **14**, 765–775.

42 S. P. Meeker, R. T. Bonnecaze and M. Cloitre, *J. Rheol.*, 2004, **48**, 1295–1320.

43 S. Marze, D. Langevin and A. Saint-Jalmes, *J. Rheol.*, 2008, **52**, 1091–1111.

44 G. Ovarlez, S. Rodts, X. Chateau and P. Coussot, *Rheol. Acta*, 2009, **48**, 831–844.

45 T. Gallot, C. Perge, V. Grenard, M.-A. Fardin, N. Taberlet and S. Manneville, *Rev. Sci. Instrum.*, 2013, **84**, 045107.

46 T. Divoux, V. Grenard and S. Manneville, *Phys. Rev. Lett.*, 2013, **110**, 018304.

47 C. W. Macosko, *Rheology: principles, measurements, and applications*, VCH, 1994.

48 I. Usov, G. Nyström, J. Adamcik, S. Handschin, C. Schütz, A. Fall, L. Bergström and R. Mezzenga, *Nat. Commun.*, 2015, **6**.

49 C. P. J. Bennington, R. J. Kerekes and J. R. Grace, *Can. J. Chem. Eng.*, 1990, **68**, 748–757.

50 C. van Wik, *J. Text. Inst.*, 1946, **37**, 285–289.

51 S. Toll and J.-A. E. Månson, *J. Rheol.*, 1994, **38**, 985–997.

52 S. Toll, *Polym. Eng. Sci.*, 1998, **38**, 1337–1350.

53 C. Servais, J.-A. E. Månson and S. Toll, *J. Rheol.*, 1999, **43**, 991–1004.

54 S. L. Corre, P. Dumont, L. Orgéas and D. Favier, *J. Rheol.*, 2005, **49**, 1029–1058.

55 J. Férec, G. Ausias, M. C. Heuzey and P. J. Carreau, *J. Rheol.*, 2009, **53**, 49–72.

56 S. Toll, *J. Rheol.*, 1993, **37**, 123–125.

57 R. G. L. Larson, *The Structure and Rheology of Complex Fluids*, Oxford University Press, New York, 1st edn, 1998.

58 S. G. Advani and C. L. Tucker II, *J. Rheol.*, 1987, **31**, 751–784.

59 G. G. Lipscomb II, M. M. Denn, D. U. Hur and D. V. Boger, *J. Non-Newtonian Fluid Mech.*, 1988, **26**, 297–325.

60 T. G. M. van de Ven, *Colloidal Hydrodynamics*, Academic Press, 1989.

61 J.-L. Barrat and L. Bocquet, *Phys. Rev. Lett.*, 1999, **82**, 4671–4674.

62 O. Guiraud, L. Orgéas, P. J. J. Dumont and S. R. du Roscoat, *J. Rheol.*, 2012, **56**, 593–623.

63 A. M. Wierenga and A. P. Philipse, *Langmuir*, 1997, **13**, 4574–4582.

64 A. Wierenga, A. P. Philipse, H. N. W. Lekkerkerker and D. V. Boger, *Langmuir*, 1998, **14**, 55–65.

65 D. Ishii, T. Saito and A. Isogai, *Biomacromolecules*, 2011, **12**, 548–550.

66 R. R. Sundararajakumar and D. L. Koch, *J. Non-Newtonian Fluid Mech.*, 1997, **73**, 205–239.

67 G. Ausias, X. J. Fan and R. I. Tanner, *J. Non-Newtonian Fluid Mech.*, 2006, **135**, 46–57.

68 P. J. J. Dumont, S. Le Corre, L. Orgéas and D. Favier, *J. Non-Newtonian Fluid Mech.*, 2009, **160**, 76–92.

69 M. P. Petrich, D. L. Koch and C. Cohen, *J. Non-Newtonian Fluid Mech.*, 2000, **95**, 101–133.

70 S. G. Advani, *Flow and Rheology in Polymer Composites Manufacturing*, Elsevier, 1994.

71 S. Wegner, T. Börzsönyi, T. Bien, G. Rose and R. Stannarius, *Soft Matter*, 2012, **8**, 10950–10958.

72 F. P. Bretherton, *J. Fluid Mech.*, 1962, **14**, 284–304.

73 L. Orgéas, P. J. J. Dumont, J.-P. Vassal, O. Guiraud, V. Michaud and D. Favier, *J. Mater. Sci.*, 2011, **47**, 2932–2942.

74 J.-P. Vassal, L. Orgéas, D. Favier, J.-L. Auriault and S. Le Corre, *Phys. Rev. E: Stat., Nonlinear, Soft Matter Phys.*, 2008, **77**, 011303.

75 M. Djalili-Moghaddam and S. Toll, *J. Non-Newtonian Fluid Mech.*, 2005, **132**, 73–83.

76 W. W. Sampson, *Modelling Stochastic Fibrous Materials with Mathematica®*, Springer Science & Business Media, 2008.

77 S. Le Corre, D. Caillerie, L. Orgéas and D. Favier, *J. Mech. Phys. Solids*, 2004, **52**, 395–421.

78 J. N. Israelachvili, *Intermolecular and Surface Forces, Third Edition: Revised Third*, Academic Press, Amsterdam, 3rd edn, 2011.

79 J. Araki, *Soft Matter*, 2013, **9**, 4125–4141.

80 L. Berhan and A. M. Sastry, *Phys. Rev. E: Stat., Nonlinear, Soft Matter Phys.*, 2007, **75**, 041121.

81 I. Balberg, C. H. Anderson, S. Alexander and N. Wagner, *Phys. Rev. B: Condens. Matter Mater. Phys.*, 1984, **30**, 3933–3943.

82 E. Abisset-Chavanne, F. Chinesta, J. Férec, G. Ausias and R. Keunings, *J. Non-Newtonian Fluid Mech.*, 2015, **222**, 34–44.